

Thermally-Induced Flexo-Type Effects in Nanopatterned Multiferroic Layers

Ronggang Cai,* Vlad-Andrei Antohe, Bernard Nysten, Luc Piraux, and Alain M. Jonas

The difficulty to generate and control large strain gradients in materials hinders the investigation and application of flexoelectricity and flexomagnetism. This work demonstrates that thermal expansion can be used to induce very large non-uniform strains at the nanoscale, resulting in giant strain gradients at moderate temperatures. This is demonstrated in a nanopatterned multiferroic hybrid layer consisting of a regular array of ferromagnetic metallic nanocylinders embedded in a ferroelectric polymer matrix. The thermally-induced strain gradients can fully depolarize the ferroelectric component, and modify the magnetization of the ferromagnetic component via flexoelectric and flexomagnetic effects, respectively. Finite-element analysis provides a quantitative view on thermal expansion-induced strains and strain gradients supporting the experimental findings. This work shows that nanoscale thermal strain engineering provides an additional degree of freedom to control electrical polarization and magnetization, which paves the way for the design and operation of novel functional devices and nanostructures.

1. Introduction

Flexo-type effects describe the coupling between functional properties of a material and strain gradients, with flexoelectricity^[1] and flexomagnetism^[2] being two typical examples. These effects are usually very weak in bulk materials and were considered to be of little practical importance for many decades after their theoretical prediction, due to the difficulty to generate the required large strain gradients in bulk materials. However, flexo-type effects have recently drawn renewed attention owing to the development of nanofabrication technology which enables the generation of large strain-gradients in

materials and devices, and of new characterization methods at the nanoscale.

In particular, the flexoelectric effect describing the coupling between electrical polarization and a strain gradient has been intensively studied over the last decade, because it may become an important way to control the electrical polarization in specific nano-designed systems, compared to other, more classically-used electromechanical effects such as piezoelectricity. Notable experimental studies were done by Catalan et al.,^[3] Kalinin et al.,^[4] and others.^[5] In addition to the study of the phenomenon itself, recent efforts have targeted the development of methods to generate sufficiently-strong strain gradients and consequently control the electrical polarization of ferroelectrics: we recently demonstrated magnetic control of the electrical polarization in multiferroic systems via

a flexoelectricity-mediated magnetoelectric effect;^[6] Lu et al. reported flexoelectrically-induced mechanical switching of the ferroelectric polarization by the probe of an atomic force microscope (AFM);^[7] and a recent paper by Liou et al. reported on the optical control of the electric polarization in multiferroic thin films by a laser beam which induced local heating and strain gradients.^[8] In these previous studies, the polarization is intrinsically regulated by a common parameter—non-uniform local mechanical strains or strain gradients in the ferroelectrics resulting from magnetostrictive deformation, mechanical force, or laser-induced local thermal strains. At the current stage, notwithstanding these notable works, a precise experimental control of the flexoelectric effect at the nanoscale remains a challenge. More work is needed to engineer strain gradients and to quantify strain gradients and electrical polarization at the nanoscale, in order to develop flexoelectricity for applications with a degree of control similar to what can be routinely achieved for piezoelectricity.

In contrast, the flexomagnetic effect, which describes the coupling between magnetization and a strain gradient, was rarely reported. A few previous works mainly focused on the theoretical prediction and numerical simulation of the flexomagnetic effect,^[2,9] but experimental support and observation of flexomagnetism remains scarce.^[10] Therefore, there is still ample room for the experimental and theoretical development of flexomagnetism and its practical applications. The reason for the rare experimental investigation of flexomagnetism might be due to the fact that most magnetic materials are

Dr. R. Cai, Prof. V.-A. Antohe, Prof. B. Nysten, Prof. L. Piraux, Prof. A. M. Jonas

Bio- and Soft Matter Research Division (BSMA)
Institute of Condensed Matter and Nanosciences (IMCN)
Université catholique de Louvain (UCLouvain)
B-1348 Louvain-la-Neuve, Belgium
E-mail: ronggang.cai@uclouvain.be

Prof. V.-A. Antohe
Research and Development Center for Materials and Electronic and Optoelectronic Devices (MDEO)
Faculty of Physics
University of Bucharest
077125 Măgurele, Ilfov, Romania

 The ORCID identification number(s) for the author(s) of this article can be found under <https://doi.org/10.1002/adfm.201910371>.

DOI: 10.1002/adfm.201910371

metals or their alloys and oxides, which are very stiff and not easily non-uniformly deformed in a well-controlled manner. As a result, it is very difficult to create large enough strains and strain gradients in these materials for generating measurable flexomagnetic effects. In order to obtain a strong flexomagnetic effect, a smarter design of material structures at the nanoscale is clearly needed to create large enough strain gradients.

Within this context, we develop here a nanopatterned multiferroic hybrid layer on a Si substrate, consisting of a ferroelectric polymer component and a ferromagnetic metal component. Our idea is to create large strain gradients in both components by thermal expansion upon heating the nanopatterned layer. This is realized by the combination of different mechanical (Young's moduli) and thermal (thermal expansion coefficients) properties of the two components and by the clamping of the bottom side of the nanostructured multiferroic layer on the much thermally-stiffer Si substrate. In this way, upon heating, the different components expand laterally with varying magnitudes in the vertical direction due to their bottom clamping, resulting in the occurrence of large vertical thermal strain gradients in both components. We demonstrate by finite-element modeling the importance of a proper nano-design of the materials, because large thermal strain gradients only extend from the interfaces of the two components over a few nanometers and at the top and/or bottom of the layer over a few tens of nanometers. We provide experimental observations of the flexoelectric effect induced by large thermal-strain gradients, which can be used to control the electrical polarization of the

ferroelectric component. Additionally, our experimental results also point to the possible existence of flexomagnetic effects in such hybrid layers, hence suggesting the possible control of the magnetization of the ferromagnetic component by thermal strain gradients.

2. Results and Discussion

2.1. Morphology and Topography of Nanopatterned Samples

The nanopatterned multiferroic composite layer was made by a parallel process reported before^[6a] and described in Section 4, involving nanoimprint lithography (NIL) and electrochemical deposition. A nanopatterned ferroelectric P(VDF-TrFE) (poly(vinylidene fluoride-*ran*-fluoroethylene)) layer obtained by NIL is schematically shown in Figure 1a. The corresponding scanning electron microscopy (SEM) and AFM images (Figure 1b,c) show that this layer is ≈ 80 nm thick with regular cylindrical holes of ≈ 65 nm diameter arranged over a square lattice of ≈ 190 nm unit cell size. The holes of this sample were then filled with Ni by electrochemical deposition. The final composite layer is schematically shown in Figure 1d. SEM (Figure 1e) and AFM (Figure 1f) images show the presence of Ni whose height is approximately the same as the thickness of the P(VDF-TrFE) continuous matrix. The diameter of the holes after NIL appears smaller in AFM compared to SEM due to tip dilation effects. Likewise, the diameter of the Ni posts appears larger in AFM than in SEM.

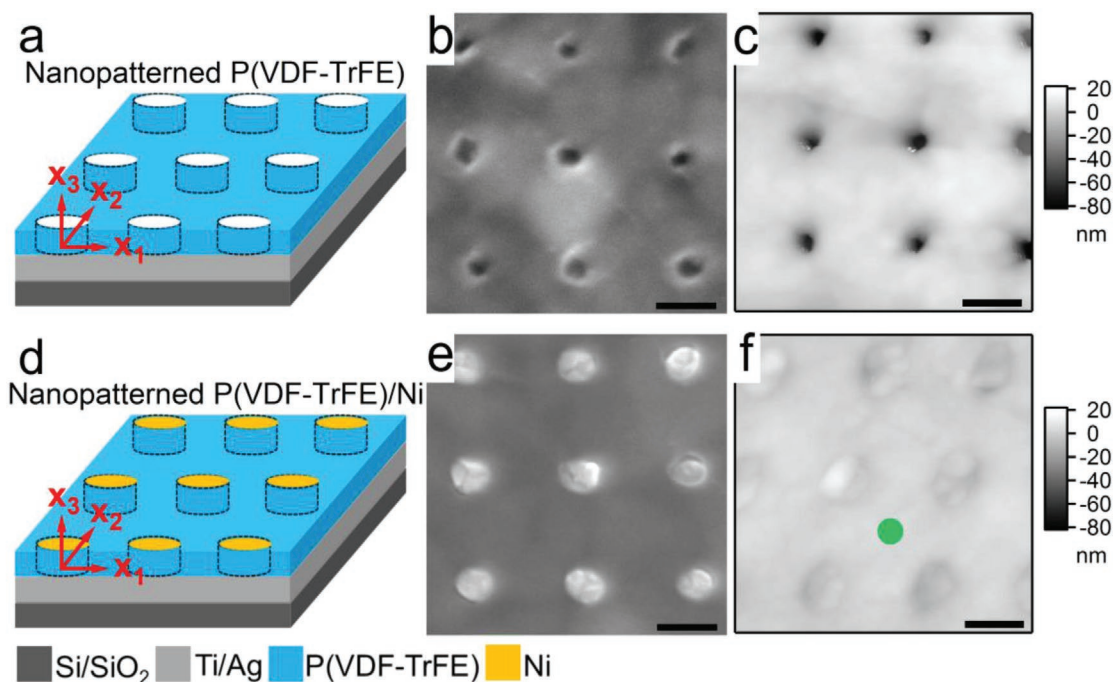


Figure 1. Nanopatterned P(VDF-TrFE) layer a–c) before and d–e) after electrochemical deposition of Ni, respectively. (a) and (d) are schematic drawings of the two samples, with indication of the reference axes. (b) and (c) are SEM and AFM images showing the morphology and topography of the nanopatterned P(VDF-TrFE) layer, respectively. (e) and (f) are SEM and AFM images showing the morphology and topography of the nanopatterned P(VDF-TrFE)/Ni hybrid layer, respectively. Scale bars in the images are 100 nm. The green dot in (f) shows the typical location of the tip when probing the local piezoelectric response as presented in Figure 3 or prepoling the ferroelectric polymer as shown in Figure 4.

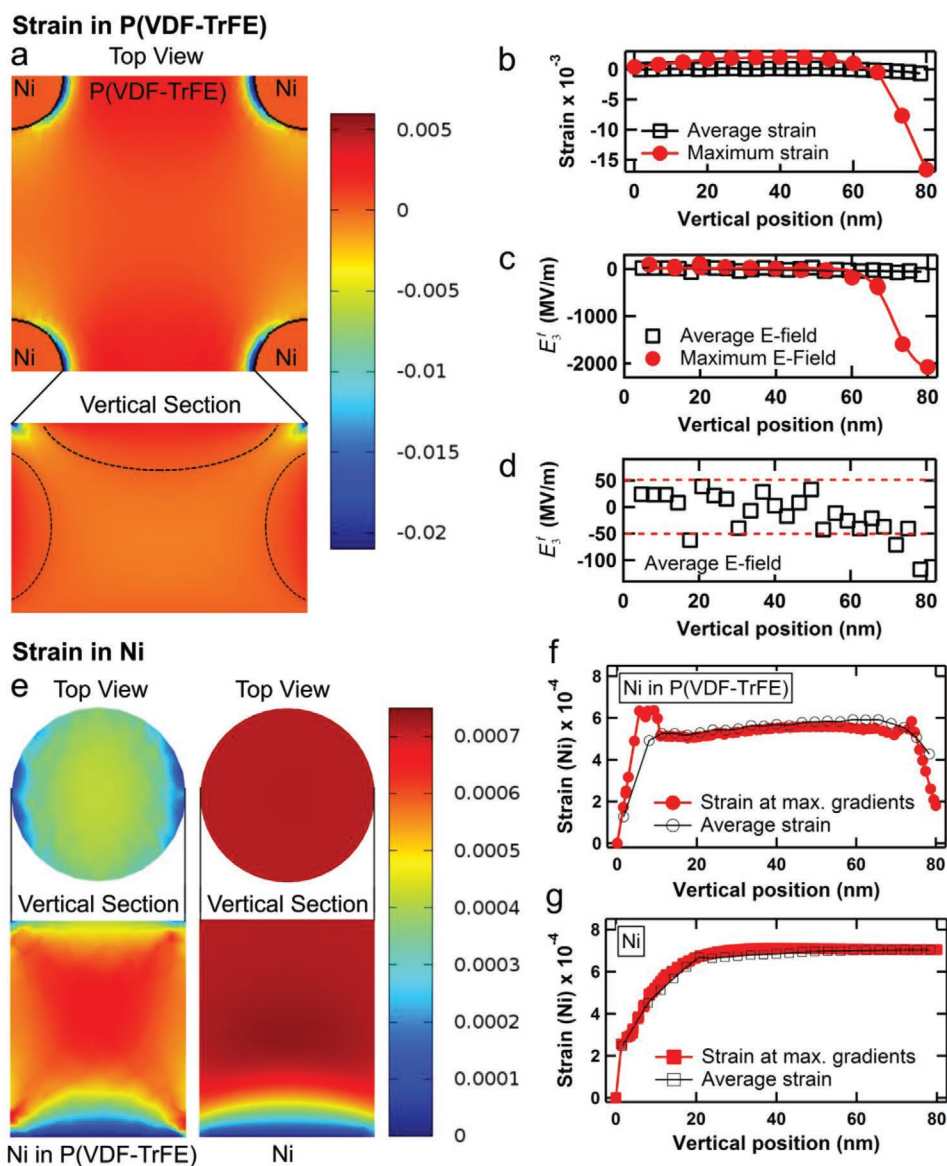


Figure 2. In-plane total strain (ϵ_{11}) induced by thermal expansion, as obtained by a finite-element model. a) Top view of ϵ_{11} in a unit cell of the composite, and cross-sectional view of ϵ_{11} in P(VDF-TrFE) along the x_1 axis of the unit cell at 60 °C. Dashed lines are used to separate expanded and compressed regions. b) Average and maximum in-plane strains in P(VDF-TrFE) at 60 °C in the vertical direction. c) Calculated average and maximum strain gradient-induced electric field E_3^f along vertical position x_3 in P(VDF-TrFE) at 60 °C. The solid lines are guides for the eyes. d) Zoom on the average electric field induced by the strain gradients also shown in (c). The dashed lines indicate an electric field magnitude of 50 MV m^{-1} , equal to the coercive field of P(VDF-TrFE). e) Top view and vertical cross-sectional view of ϵ_{11} in Ni cylinders (left: when embedded in P(VDF-TrFE) matrix; right: after removal of P(VDF-TrFE)) at 75 °C. f) Average strains and strains at the location of maximal gradient in Ni cylinders (embedded in a P(VDF-TrFE) matrix) at 75 °C, along vertical position x_3 . g) Same as (f), after removal of the P(VDF-TrFE) matrix.

2.2. Strains Induced by Thermal Expansion in the Ferroelectric P(VDF-TrFE) and Ferromagnetic Ni Components

Finite-element analysis (COMSOL Multiphysics) was first performed to have a quantitative estimation on the distribution and magnitude of strains and strain gradients induced by thermal expansion in both the polymer and metal components of the nanopatterned multiferroic layer. The specific conditions and material parameters of P(VDF-TrFE) and Ni used for the simulation are described in Section 4. We concentrate on the in-plane normal strain $\epsilon_{11} = \epsilon_{22}$ since its vertical gradient has a dominant

effect on the vertical electrical polarization and magnetization which are characterized in this work. The gradient of out-of-plane strain ϵ_{33} is much smaller than that of ϵ_{11} (Figure S1, Supporting Information), especially in the top part of the layer where the polarizations are characterized in this work. Therefore, we do not discuss the strain gradient of ϵ_{33} in the main text, nor the ones of the shear strains ϵ_{13} and ϵ_{23} (Figure S1, Supporting Information) which similarly can be neglected.

The distribution and magnitude of the total in-plane strain ϵ_{11} induced by thermal expansion at 60 °C in the P(VDF-TrFE) component is shown in **Figure 2a**. The top view map and the

vertical section indicate that the thermal strains are extremely non-uniform, leading to large strain gradients at specific locations in the structure. Large negative strains concentrate in the upper part of the layer around the Ni cylinders. Positive strains appear in regions surrounded by the dashed lines in the vertical section. The maximum and unit-cell-average values of thermal in-plane strains in P(VDF-TrFE) are plotted in Figure 2b versus the vertical position from the bottom (x_3 axis in Figure 1). The strain and vertical strain gradient are non-uniform, with large strain gradients concentrating over the upper 10–20 nm of the layer. The maximum in-plane strain and vertical gradient of the in-plane strain ($\partial\epsilon_{11}/\partial x_3$) can reach values as high as -1.66×10^{-2} and $-1.35 \mu\text{m}^{-1}$, respectively, 2–3 orders of magnitude larger than the ones which can be induced by magnetostrictive deformations of Ni as we reported before.^[6] We expect that these large thermal-strain gradients could be strong enough to switch the electrical polarization of P(VDF-TrFE). The equivalent flexoelectricity-generated downward-pointing electric field E_3^f can be calculated from the equation $E_3^f = f_{3311}(\partial\epsilon_{11}/\partial x_3) \approx (\mu_{3311}/\chi\epsilon_0)(\partial\epsilon_{11}/\partial x_3)$,^[11] with f_{3311} and μ_{3311} the flexoelectric coupling coefficient and flexoelectric coefficient of P(VDF-TrFE), respectively, $\chi \approx 14$ the dielectric susceptibility of P(VDF-TrFE),^[11] and $\epsilon_0 = 8.854 \times 10^{-12} \text{ F m}^{-1}$ the dielectric permittivity of the vacuum. Taking $191 \times 10^{-9} \text{ C m}^{-1}$ for the flexoelectric coefficient μ of P(VDF-TrFE),^[5f] the average and maximum values of flexoelectrically-induced vertical electric field E_3^f can be computed at each position (Figure 2c).

In the upper 10–20 nm of the layer, the maximum E_3^f values are much larger than average ones and can reach values as high as $\approx 2000 \text{ MV m}^{-1}$, well exceeding the coercive field of P(VDF-TrFE) layers of $\approx 80 \text{ nm}$ thickness which is $\approx 50 \text{ MV m}^{-1}$,^[12] and large enough to locally switch the electric polarization. It is obvious that such large values of field are not physically possible. Instead, relaxation processes will be undertaken by the polymer chains, including mechanical relaxation and polarization switching, to avoid a local excess of mechanical and electrostatic energy. Furthermore, the maximum value of the vertical gradient of the out-of-plane strain ϵ_{33} reaches $0.32 \mu\text{m}^{-1}$ (Figure S1, Supporting Information). Although more than four times smaller than the one of the in-plane strain gradient, it contributes to relax the large mechanical and electrostatic energy generated by the larger gradient of in-plane strain, since it acts in the opposite direction.

The average absolute value of E_3^f (Figure 2d) also exceeds the coercive field threshold of 50 MV m^{-1} in the upper $\approx 10 \text{ nm}$ of the ferroelectric layer, which is again sufficient to initiate the switching of the ferroelectric polarization. Even though large values of flexoelectrically-induced vertical field E_3^f are only present in small regions, one should note that polarization switching involves a process of domain nucleation and propagation.^[13] As domain nucleation starts at the local position of the maximum field, local values of electric fields should be considered for the initiation of domain reversal, rather than average values. Once the nucleation event is activated, the switched ferroelectric domains propagate both laterally and vertically at lower values of the electric field.^[14] This will be confirmed by the experimental observations presented below.

The distribution and magnitude of the in-plane strain ϵ_{11} in the Ni component embedded in the nanopatterned

P(VDF-TrFE) layer is shown in Figure 2e (left), at $75 \text{ }^\circ\text{C}$. When reading these maps, one should not forget the existence of an in-plane strain ϵ_{22} of identical magnitude in the Ni cylinders (not shown), leading to the expected cylindrical symmetry of $(\epsilon_{11}^2 + \epsilon_{22}^2)^{1/2}$. The top view map and the vertical section indicate that the thermally-induced in-plane strains are again extremely non-uniform, with larger strains concentrating in the middle of the cylinders, while vertical strain gradients concentrate at their clamped bottom and top surfaces. Strains at the location of the maximum vertical strain gradient, and average strains, are plotted versus vertical position x_3 in Figure 2f. Large strain gradients extend over $\approx 10 \text{ nm}$ from both ends of the nanocylinders.

The maximum value of the vertical gradient of in-plane strain can reach values as high as $0.11 \mu\text{m}^{-1}$ in the 0–10 nm vertical range (bottom part of the Ni cylinders) and $-0.07 \mu\text{m}^{-1}$ in the 70–80 nm range (top part of the Ni cylinders). The average gradient values are $\approx 0.06 \mu\text{m}^{-1}$ and $-0.02 \mu\text{m}^{-1}$ in the same vertical ranges, respectively. The distribution and magnitude of the in-plane strain ϵ_{11} in Ni is also shown in Figure 2e (right) for a reference sample consisting of only Ni nanocylinders with the P(VDF-TrFE) removed. In this reference sample, large strain gradients are only present at the bottom of the cylinder due to the clamping effect while all other regions expand freely more uniformly. The extracted values of strains at maximum gradient and average strains versus vertical position are also plotted in Figure 2g. The two curves are identical, demonstrating lateral homogeneity of the strain gradients, which are in the range of $0.02\text{--}0.03 \mu\text{m}^{-1}$ over the first 15 nm of the feet of the cylinders. Note that these values are ≈ 5 orders of magnitude larger than the ones reported in a recent paper, in which a strain gradient of at most $\approx 2 \times 10^{-7} \mu\text{m}^{-1}$ was generated by bending, resulting in the flexomagnetic induction of magnetic anisotropy in a thin permalloy film.^[10a] Therefore, the much larger strain gradients generated in Ni by the thermal expansion of our nanostructured system could possibly affect the magnetization of Ni as well.

2.3. Flexoelectric Control of the Electrical Polarization of Ferroelectric P(VDF-TrFE) by Thermal Strain Gradients

The local ferroelectric response of the P(VDF-TrFE) component in the nanopatterned composite was characterized by piezoresponse force microscopy (PFM) at different temperatures, with the PFM tip placed at the center of a unit cell as indicated by the green dot in Figure 1f. The bias was applied on the tip while the bottom electrode was grounded, resulting in a downward-pointing electric field for positive tip biases, and vice-versa. Due to the large thermal strain gradients (Figure 2a), the electrical polarization of P(VDF-TrFE) is expected to be strongly altered or even completely switched when increasing temperature. The vertical PFM phase and amplitude curves (Figure 3a,b) show that electrical polarization switching of P(VDF-TrFE) indeed strongly depends on temperature. The ferroelectric hysteresis loop width (FHLW, Figure 3a) decreases significantly when temperature increases, for example, from $\approx 4 \text{ V}$ at $25 \text{ }^\circ\text{C}$ to $\approx 2.5 \text{ V}$ at $55 \text{ }^\circ\text{C}$. The phase hysteresis and amplitude butterfly shape are not observed above $95 \text{ }^\circ\text{C}$ because this temperature exceeds the Curie point of P(VDF-TrFE) (Figure S1, Supporting

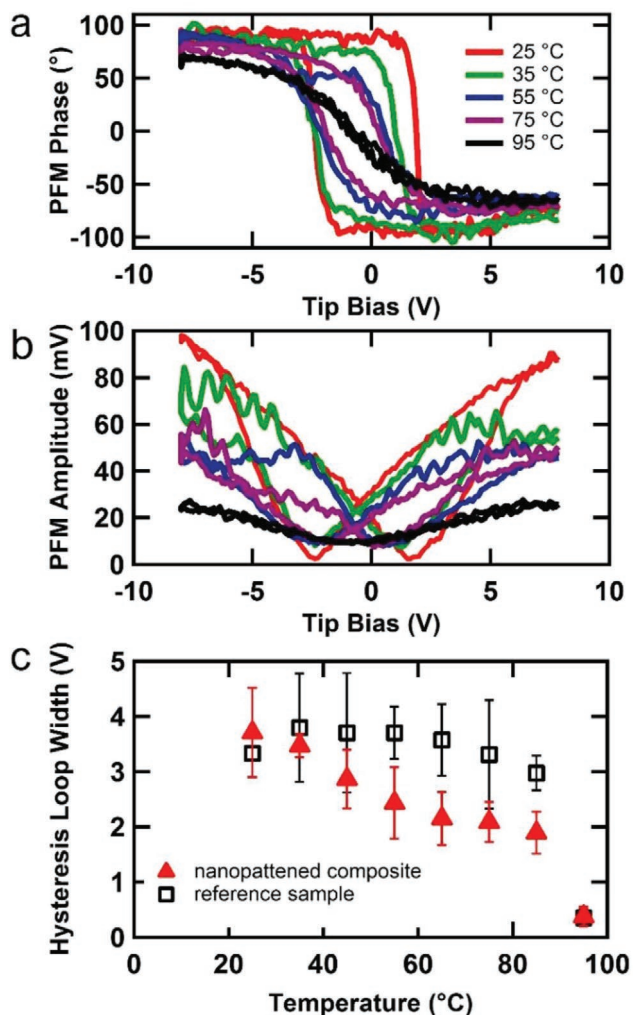


Figure 3. Local vertical PFM response (a) phase and b) amplitude) of a nanopatterned P(VDF-TrFE)/Ni sample at different temperatures. The average width of the PFM phase hysteresis loops at different temperatures are shown in (c) for the nanopatterned P(VDF-TrFE)/Ni sample and a reference nanopatterned P(VDF-TrFE) sample. The average width values were calculated based on measurements done at five different locations.

Information) resulting in the loss of ferroelectricity. Interestingly, the decrease of FHLW essentially happens on the positive bias side of the loops, suggesting that higher temperatures create an added downward-pointing electric field which decreases the bias required to switch the polarization from up- to downwards. Our hypothesis is that this downward field corresponds to the flexoelectrically-induced field E_3^f .

The average values of FHLW obtained from the tests at five different locations at different temperatures are shown in Figure 3c (red solid triangles). They are compared in Figure 3c with the values measured on a reference nanopatterned P(VDF-TrFE) sample devoid of Ni (Figure 1a–c). The corresponding PFM hysteresis curves are in Figure S3, Supporting Information. The FHLW of the reference sample remains approximately constant up to 65 °C (open squares in Figure 3c) and it only starts to decrease at higher temperatures, in the thermal range of the broad Curie transition detected

by differential scanning calorimetry (Figure S2, Supporting Information). This indicates that the significant decrease of the FHLW in our nanopatterned composite is not arising from the temperature-dependence of the ferroelectric properties of P(VDF-TrFE), but originates from the joint presence of P(VDF-TrFE) and the Ni nanocylinders which creates strong strain gradients due to differential thermal expansion, resulting in the easier switching of an upward-pointing polarization.

To further probe these thermal effects, vertical PFM images were recorded at different temperatures over an area of 650 nm² size in which two regions were pre-poled by a –8 V tip bias resulting in upward polarization and two regions by a 8 V bias resulting in downward polarization (red and blue dots in the first topography image of Figure 4a, respectively). Red (respectively, blue) arrows in PFM amplitude images point to the regions where polarization was initially pointing upwards (respectively, downwards). To have a more quantitative view on how polarization is affected by heating, the PFM amplitude and phase contrasts were extracted for the upward- and downward-pointing polarized regions, respectively. The contrasts were defined as the absolute differences of amplitude or phase values measured along lines crossing the pre-poled (red and blue dots in Figure 4a) and unpoled regions (green dot in Figure 4a). The evolution of the amplitude contrast for initially upward- or downward-pointing polarizations are shown in Figure 4b.

In the case of an upward-pointing polarization (red squares in the top panel of Figure 4b), a clear amplitude contrast exists between poled and unpoled regions at 22.5 °C. This amplitude contrast decreases when temperature increases and disappears progressively until temperature reaches ≈60 °C, well below the Curie transition of the polymer. In contrast, when the reference sample is measured in the same way (open black squares in the top panel of Figure 4b), the amplitude contrast remains approximately constant until ≈80 °C, from which it progressively disappears due to the loss of polarization arising in the Curie transition region. This again provides a strong support for the existence of a downward-pointing depolarizing flexoelectric field E_3^f , which increases in strength with temperature in the composite nanostructure and is absent in the reference sample.

In the case of a downward-pointing polarization (red circles in the bottom panel of Figure 4b), a clear contrast between poled and unpoled regions can be observed in the PFM phase image at 22.5 °C (red circles). The contrast first increases when temperature increases until reaching a maximum value at ≈70 °C, indicating that the downwards polarization is progressively better aligned in the vertical direction. The phase contrast then slightly decreases with temperature above 70 °C due to the beginning of the Curie transition of P(VDF-TrFE). The phase contrast is lost at the Curie point of P(VDF-TrFE). A similar temperature-variation of the phase contrast is observed for the reference sample devoid of Ni (open black circles in the bottom panel of Figure 4b), except for the increase of the contrast with temperature below 70 °C which does not exist in the absence of Ni. Again, these observations are fully consistent with the existence of a downward-pointing electric field E_3^f , which contributes to slightly enhance the downward polarization in the nanocomposite layer.

The asymmetry of the temperature effect depending on whether the polarization is initially upward- or

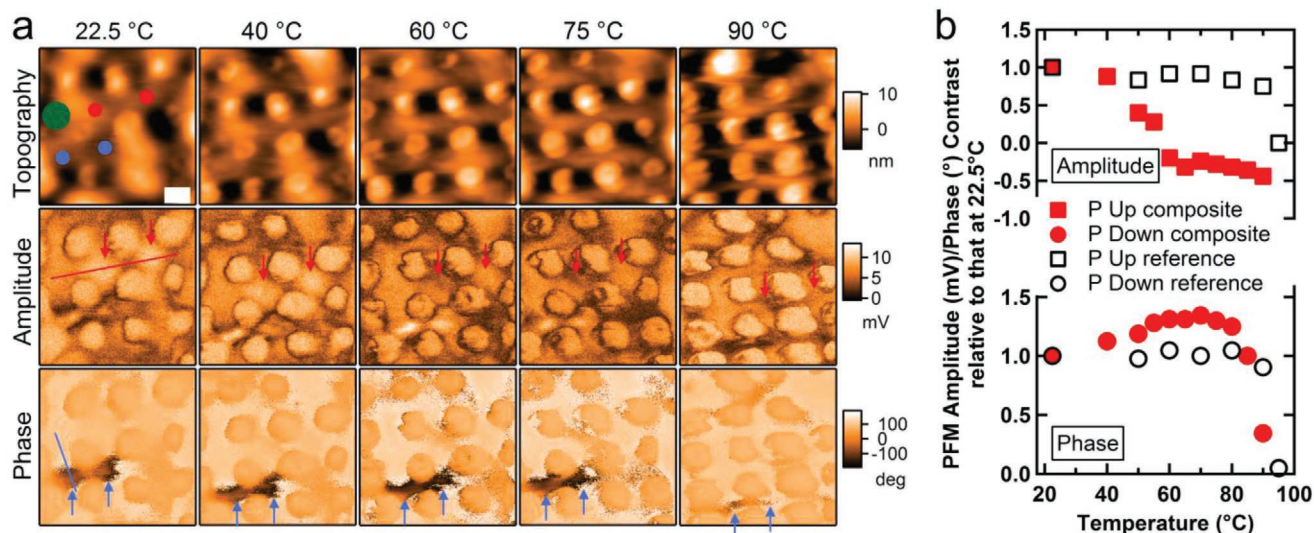


Figure 4. Temperature switching of the electrical polarization of a pre-poled nanopatterned P(VDF-TrFE)/Ni sample. a) PFM topography, vertical PFM amplitude and phase images at five different temperatures (five columns) are shown in the first, second, and third rows, respectively. The scale bar shown in the first topography image is 100 nm and is applicable to all fifteen images. The circular regions in all images indicate the position of Ni cylinders, which appear broader than in reality due to tip dilation effects. The red and blue dots in the first topography image represent the locations where the ferroelectric polymer was poled by applying -8 or 8 V for 4 s to the PFM tip at 22.5 °C, respectively. The background was unpoled. The green dot represents a reference unpoled region taken as reference to calculate the amplitude and phase contrast between the poled and unpoled regions. Red and blue arrows in amplitude and phase images indicate the regions poled by -8 and 8 V tip bias, respectively. b) Vertical PFM amplitude contrast for upward polarization (poled by a -8 V tip bias) and vertical PFM phase contrast for downward polarization (poled by a 8 V tip bias) extracted from PFM amplitude and phase images presented in (a). Data obtained from tests done on the reference sample (nanopatterned P(VDF-TrFE) without Ni) was also added for comparison (vertical PFM amplitude and phase images of the reference sample at different temperatures are shown in Figure S4, Supporting Information).

downward-pointing is in good agreement with our finite-element modeling results, and fully supports flexoelectricity as being the cause for the observations in the nanocomposite layer. The temperature dependence of the effect is also in agreement with the predicted strain gradients in the composite layer, which are not present in the reference sample. Nevertheless, one might argue that the thermal expansion-induced stresses (σ) in P(VDF-TrFE) may play a role in the polarization switching via the piezoelectric effect. However, from the finite-element simulation (Figure S5, Supporting Information), we found that the in-plane stresses (σ_{11}) in P(VDF-TrFE) range from -3.7×10^7 to -1×10^7 N m $^{-2}$ with an average value of $\approx -1.5 \times 10^7$ N m $^{-2}$, whereas the out-of-plane stress σ_{33} ranges from -1.5×10^7 to 0.3×10^7 N m $^{-2}$ with an average of $\approx -0.4 \times 10^7$ N m $^{-2}$. The piezoelectricity-induced equivalent electric field E_3^p can then be estimated from $E_3^p \approx d\sigma/\chi\epsilon_0$ with $d \approx 20 \times 10^{-12}$ C N $^{-1}$ the piezoelectric coefficient of P(VDF-TrFE), leading to a field of a few MV m $^{-1}$ at most, significantly smaller than the coercive field of P(VDF-TrFE). Consequently, the thermally-induced piezoelectric effect can be safely neglected compared to the much larger thermally-induced flexoelectric effect in the nanopatterned composite.

2.4. Possible Control of the Magnetization of Ferromagnetic Ni by Thermal Strain Gradients via the Flexomagnetic Effect

The simulation shown in Figure 2e indicates the presence of large thermal strain gradients in the Ni cylinders that might

result in a significant change of the local magnetic anisotropy by the flexomagnetic effect. To investigate this, two nanopatterned samples were characterized by magnetic force microscopy (MFM). Sample 1 is a nanopatterned multiferroic P(VDF-TrFE)/Ni layer with a height of Ni nanocylinders of ≈ 65 – 70 nm, 10 – 15 nm lower than the P(VDF-TrFE) matrix, prepared using the same process as for the multiferroic sample shown in Figure 1. Sample 2 only consists of ferromagnetic Ni nanocylinders prepared from Sample 1 with the P(VDF-TrFE) removed by dissolution in acetone. Prior to MFM characterization, both samples were placed in a 1 T magnetic field for pre-magnetization in the out-of-plane direction (upwards) at room temperature (≈ 22.5 °C). One should note that, given the size and aspect-ratio of the cylinders, the stable magnetic state could either be a vortex state with a residual upwards magnetization at the center, or a “flower” state, both of which of low remanent polarization.^[15] The MFM magnetic probe was also magnetized in the same direction and the magnetic force between samples and the probe was thus initially attractive. The topography and MFM phase-shift images of the two samples are shown in Figure 5a,b for different temperatures. In the harmonic oscillator approximation, MFM phase-shift is inversely proportional to the magnetic force gradient ($\Delta\phi \propto -\frac{Q}{k} \frac{\partial F}{\partial x_3}$, where Q is the quality factor of the cantilever, k its stiffness, F is the magnetic force between the probe and the sample, and x_3 is the axis coordinate in the vertical direction).^[16] Therefore, attractive forces with a positive gradient lead to a negative phase-shift (dark contrast) and repulsive forces with a negative gradient lead to a positive

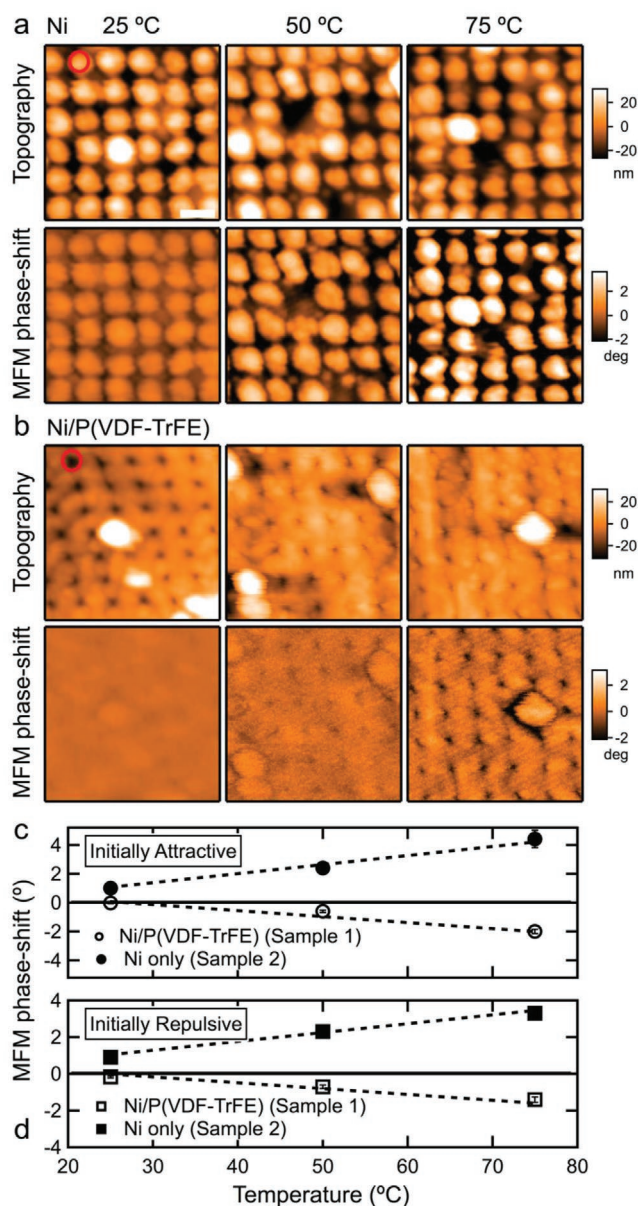


Figure 5. MFM characterization of two nanopatterned samples at different temperatures. a) Topography and MFM images for the ferromagnetic sample consisting of only Ni nanocylinders. b) Topography and MFM images for the multiferroic sample with Ni nanocylinders embedded in a P(VDF-TrFE) matrix. Red circles in Panels (a) and (b) show the typical positions of Ni-cylinders. Due to tip dilation, protruding cylinders in the Ni-only sample appear much bigger than partially Ni-filled holes in the composite sample. Panel (c) shows MFM phase-shifts on top of Ni regions compared to the surrounding background, plotted versus temperature for both samples, when the samples and probe were pre-magnetized upwards in a 1 T field in the same direction (resulting in an initially-attractive force between them). Panel (d) represents the case when the samples and probe are pre-magnetized in opposite directions with a downwards orientation of the vertical magnetization in Ni, resulting in an initially-repulsive force.

phase-shift (bright contrast). Since our samples and the probe were pre-magnetized in the same direction (upwards), the initial force between them is attractive. Therefore, a negative phase shift

(dark contrast) compared to that measured on the non-magnetic background should be obtained. This is the case for the nanopatterned multiferroic sample comprising a P(VDF-TrFE) matrix as shown in the MFM phase-shift images of Figure 5b.

However, at 25 °C, close to room temperature, the dark contrast is very small (close to zero), which results from the fact that the out-of-plane remanent magnetization (Figure S6, Supporting Information) is too small to be effectively sensed by the probe at 50 nm lift height (the condition used for sensing the force between the probe and Ni). Interestingly, the dark contrast increases with increasing temperature, indicating that the magnetic force between the sample and the probe increases: the magnetization of the Ni nanocylinders is thus steadily enhanced with temperature in the vertical direction, which we ascribe to flexomagnetism arising from the large negative strain gradients existing in the upper part of the nanocylinders, as shown in Figure 2e. Although large positive strain gradients also exist at the bottom of the cylinders, which should play an opposite role, their larger distance from the MFM tip results in the dominance of the top strain gradients in the MFM signal.

Consistently, the MFM phase-shift is completely different for the sample consisting of Ni nanocylinders only, as shown in Figure 5a. Instead of a dark phase-shift contrast, a bright contrast compared to that measured on the non-magnetic background is now obtained, which increases with increasing temperature. Again, the MFM phase-shift values are small at 25 °C due to the small remanent magnetization as explained above. When temperature increases, as simulated in Figure 2e, large strain gradients are only generated in the lower part of the Ni cylinders, because the top part of the cylinders is now unconstrained. This positive bottom gradient now becomes the dominant temperature-dependent factor controlling the magnetization in the vertical direction. Because these large strain gradients are positive, the magnetic dipoles in the nanocylinders tend to align in the opposite direction as those of the probe, resulting in a temperature-enhanced bright contrast.

Figure 5c (top) also presents the MFM phase-shifts versus temperature (circles). They vary linearly with temperature in opposite directions for the two samples, as expected from the fact that thermal expansion is a linear phenomenon, in agreement with previous reports on flexomagnetism.^[9a,10a] We also pre-magnetized samples and probe in 1 T magnetic fields of opposite directions, leading to an initially-repulsive force between them. Here, the orientation of the magnetization in Ni (downwards) is opposite to the previous one. In this case, the same observations were obtained by MFM as can be seen in Figure 5d (bottom), in which the MFM phase-shifts measured with respect to the surrounding background are plotted versus temperature. The enhancement of the magnetization of the Ni nanocylinders in the vertical direction is identical to the previous case of initially-attracting probe and Ni cylinders, and is thus independent of the initial magnetic state of Ni, which might result from the possible existence of a vortex structure in the Ni nanocylinders.^[15b] This is again in good agreement with expectations based on a flexomagnetically-induced temperature variation of the magnetization, since the strain gradients are independent of the initial magnetization state of Ni.

One may wonder whether inverse magnetostriction does not play a more dominant role in the observed thermal variations

of the out-of-plane magnetization, as was reported for much longer Ni nanowires embedded in polymer templates, for which interfacial strain gradients play a much less important role.^[17] Ni has a negative magnetostrictive coefficient at saturation $\lambda_s \approx -3.5 \times 10^{-5}$.^[18] Therefore, since in-plane stresses σ_{11} are essentially negative in the polymer-embedded Ni nanocylinders (Figure S5, Supporting Information), magnetostriction should tend to tilt the magnetization in the horizontal direction. Likewise, out-of-plane stresses σ_{33} are essentially positive in the polymer-embedded Ni nanocylinders (Figure S5, Supporting Information). Therefore, magnetostriction should tend to tilt the magnetization away from the vertical direction. As a consequence, magnetostriction should result in a decrease of the out-of-plane magnetization, whereas it is increased in our experiments performed on embedded nanowires.

3. Conclusions

In summary, we have developed nanopatterned multiferroic hybrid layers consisting of a ferroelectric and a ferromagnetic component. We have demonstrated quantitatively by finite-element simulation that large vertical thermal strain gradients can be generated in both materials, due to the differential thermal expansion of the two components. We have experimentally observed that these large thermal strain gradients create a downward-pointing depolarizing electric field via a strong flexoelectric effect, which strongly decreases the electrical polarization of the ferroelectric component and eases its switching. This provides a new way to thermally control the local electrical properties of multiferroic materials via flexoelectricity, which may enable the design and operation of novel functional devices and structures. Importantly, we have also provided experimental evidence supporting the existence in our nanostructured layers of the previously-rarely-reported flexomagnetic effect, resulting in an increase of the magnetization in the ferromagnetic component upon heating. Although a complete demonstration of this effect would require further investigations, our results point to the possible co-existence of flexoelectric and flexomagnetic effects in multiferroic nanostructured thin films, which opens perspectives for a more general application of flexo-type phenomena.

Clearly, it is possible to design materials at the nanoscale in the aim of enhancing flexo-type effects, owing to the significance of thermal expansion at the nanometer scale. We have observed that large strain gradients only concentrate in regions of $\approx(10\text{--}20\text{ nm})$ size on the upper and/or lower interfaces in our samples of $\approx 200\text{ nm}$ unit cell dimension. Therefore, reducing by a factor of ten the unit cell dimensions would reduce the regions of high strain gradients to 1–2 nm, while simultaneously increasing the strain gradients further by a factor of ten. There is thus room for further amplification of flexo-type effects induced by thermal strain gradients, which may result in an even easier control or switching of electrical polarization and magnetization than in the present work. Of note, large thermal strain gradients would be created in the ferroelectric polymer by nanocylinders of any hard nanomaterial displaying similar Young's modulus and thermal expansion coefficient as Ni, including non-magnetic materials; likewise,

thermal strain gradients would be generated in Ni nanocylinders by any polymer layer, not necessarily a ferroelectric layer. Therefore, the applicability of our findings goes well beyond the field of magnetoelectric materials.

4. Experimental Section

Materials and Fabrication of the Nanopatterned Layer: Si wafers with a 200 nm thick SiO₂ layer were used as substrates. A 10/100 nm Ti/Ag bi-layer was deposited by electron-beam evaporation as the bottom electrode on the substrate. Then, a $\approx 75\text{ nm}$ P(VDF-TrFE) layer was spin-coated from a P(VDF-TrFE)/acetone solution (35 g L⁻¹, 6500 rpm for 1 min, P(VDF-TrFE) 65/35 wt% of VDF/TrFE units, $M_w \approx 300\,000\text{ g mol}^{-1}$, Solvay Specialty Polymers). After this, the nanopatterns were produced by nanoimprinting performed on the P(VDF-TrFE) layer with an Obducat nanoimprinter (135 °C, 60 bar, 10 min) using a Si mold with pillars arranged over a bi-dimensional square lattice of 190 nm unit cell dimension. The pillar diameter and height were 65 nm and 90 nm, respectively. Then, Ni cylinders of $\approx 80\text{ nm}$ height were grown by pulsed electrochemical deposition (-1.05 V for 10 ms and -0.7 V for 90 ms) from an aqueous electrolyte bath containing 0.5 M NiSO₄·6H₂O and 0.4 M H₃BO₃, at room temperature, with a total process duration of about 1.5 min. The chemicals were of analytical grade (Sigma-Aldrich) and they were used as provided, without further purification. During the electrochemical growth of Ni nanocylinders, the potential sequence was applied by a PAR 263A Potentiostat against a double junction Ag/AgCl reference electrode (KCl saturated, $E = 0.197\text{ V}$ versus SHE—Standard Hydrogen Electrode), while a Pt foil was installed in the bath as a counter electrode. The reference sample was a nanopatterned P(VDF-TrFE) layer without electrochemical deposition of Ni.

Characterization of the Nanopatterned Layer: The topography and morphology of the sample was characterized by atomic force microscopy (AFM, Bruker ICON Dimension) in tapping mode and by field-emission scanning electron microscopy (SEM, JEOL 7600F) in secondary electron imaging mode, respectively. The ferroelectric response of P(VDF-TrFE) was characterized by piezoresponse force microscopy (PFM) under a $\approx 25\text{ nN}$ contact force between the tip and the sample. A conductive Pt/Ir coated probe was employed (SCM-PIT-V2 from Bruker). The resonance contact frequency of this tip was $\approx 280\text{ kHz}$. Poling of the ferroelectric polymer was done by applying a DC voltage to the tip while keeping the bottom electrode grounded. The PFM data acquisition was done by applying an AC voltage of 2 V amplitude and 260 kHz contact frequency to the bottom electrode. The magnetic response of Ni was characterized by magnetic force microscopy (MFM) using a two-pass procedure. First, the topography of one line was recorded in standard intermittent-contact mode. Then, the AFM probe was lifted by 50 nm and the same line was scanned at a constant 50 nm probe-surface distance. The phase-shift signal (proportional to the magnetic force interaction) was simultaneously recorded. The probe used for MFM is Co/Cr coated (MESP-HM from Bruker) and was pre-magnetized in a 1 T magnetic field before characterization. The temperature of the sample was controlled by an auto-tuning temperature controller (LakeShore 321).

COMSOL Simulation: The P(VDF-TrFE)/Ni composite layer and the Ni nanocylinders alone (P(VDF-TrFE) removed) were simulated and meshed by combining modules of structural mechanics and heat transfer. The Si/SiO₂ substrate and Ti/Ag electrode layers were not included in the mesh, considering the very small thermal expansion of Si 16 unit cells (4 columns \times 4 rows) were used in the mesh. In order to avoid the inaccurate strain values in regions close to the edge of the 12 external cells, the thermally-induced strains/strain-gradients were obtained from the four central unit cells, which are identical by symmetry. The initial temperature was set to be 22.5 °C and the thermally-induced strains/strain-gradients were evaluated at higher temperatures. The bottom of the P(VDF-TrFE)/Ni layer was assumed to be fully clamped because the thermal expansion coefficient of Si/SiO₂ is extremely small compared to the ones of P(VDF-TrFE) and Ni. It was also assumed that the sample

was under unstrained condition at room temperature (22.5 °C). The characteristic parameters of P(VDF-TrFE) and Ni used for the simulation are listed in Table S1, Supporting Information.

Supporting Information

Supporting Information is available from the Wiley Online Library or from the author.

Acknowledgements

The authors thank Prof. Laurent Delannay for assistance in the finite-element analysis and Solvay Specialty Polymers for providing P(VDF-TrFE) copolymers.

Conflict of Interest

The authors declare no conflict of interest.

Keywords

flexoelectricity, flexomagnetism, nanopatterned multiferroic layers, thermally-induced strain gradients

Received: December 13, 2019

Revised: January 20, 2020

Published online:

- [1] B. Wang, Y. Gu, S. Zhang, L.-Q. Chen, *Prog. Mater. Sci.* **2019**, *106*, 100570.
- [2] E. A. Eliseev, A. N. Morozovska, M. D. Glinchuk, R. Blinc, *Phys. Rev. B* **2009**, *79*, 165433.
- [3] a) G. Catalan, A. Lubk, A. H. G. Vlooswijk, E. Snoeck, C. Magen, A. Janssens, G. Rispens, G. Rijnders, D. H. A. Blank, B. Noheda, *Nat. Mater.* **2011**, *10*, 963; b) P. Zubko, G. Catalan, A. K. Tagantsev, *Annu. Rev. Mater. Res.* **2013**, *43*, 387; c) U. K. Bhaskar, N. Banerjee, A. Abdollahi, Z. Wang, D. G. Schlom, G. Rijnders, G. Catalan, *Nat. Nanotechnol.* **2016**, *11*, 263; d) J. Narvaez, F. Vazquez-Sancho, G. Catalan, *Nature* **2016**, *538*, 219; e) F. Vazquez-Sancho, A. Abdollahi, D. Damjanovic, G. Catalan, *Adv. Mater.* **2018**, *30*, 1705316; f) P. Vales-Castro, K. Roleder, L. Zhao, J.-F. Li, D. Kajewski, G. Catalan, *Appl. Phys. Lett.* **2018**, *113*, 132903.
- [4] a) S. V. Kalinin, V. Meunier, *Phys. Rev. B* **2008**, *77*, 033403; b) Q. Li, C. T. Nelson, S. L. Hsu, A. R. Damodaran, L. L. Li, A. K. Yadav, M. McCarter, L. W. Martin, R. Ramesh, S. V. Kalinin, *Nat. Commun.* **2017**, *8*, 1468.
- [5] a) B. Chu, D. R. Salem, *Appl. Phys. Lett.* **2012**, *101*, 103905; b) J. Brahmanandam, H. Bo, Z. Xiaoying, *Nanotechnology* **2018**, *29*, 225702; c) U. Celano, M. Popovici, K. Florent, S. Lavizzari, P. Favia, K. Paulussen, H. Bender, L. di Piazza, J. Van Houdt, W. Vandervorst, *Nanoscale* **2018**, *10*, 8471; d) X. Hu, Y. Zhou, J. Liu, B. Chu, *J. Appl. Phys.* **2018**, *123*, 154101; e) J.-H. Liu, X. Chen, Y. Li, X. Guo, H.-X. Ge, Q.-D. Shen, *Appl. Phys. Lett.* **2018**, *113*, 042903; f) S. Poddar, S. Ducharme, *Appl. Phys. Lett.* **2013**, *103*, 202901; g) S. Poddar, S. Ducharme, *J. Appl. Phys.* **2014**, *116*, 114105.
- [6] a) R. Cai, V.-A. Antohe, Z. Hu, B. Nysten, L. Piraux, A. M. Jonas, *Adv. Mater.* **2017**, *29*, 1604604; b) S. Poddar, P. de Sa, R. Cai, L. Delannay, B. Nysten, L. Piraux, A. M. Jonas, *ACS Nano* **2018**, *12*, 576.
- [7] H. Lu, C.-W. Bark, D. Esque de los Ojos, J. Alcalá, C. B. Eom, G. Catalan, A. Gruverman, *Science* **2012**, *336*, 59.
- [8] Y.-D. Liou, Y.-Y. Chiu, R. T. Hart, C.-Y. Kuo, Y.-L. Huang, Y.-C. Wu, R. V. Chopdekar, H.-J. Liu, A. Tanaka, C.-T. Chen, C.-F. Chang, L. H. Tjeng, Y. Cao, V. Nagarajan, Y.-H. Chu, Y.-C. Chen, J.-C. Yang, *Nat. Mater.* **2019**, *18*, 580.
- [9] a) P. Lukashev, R. F. Sabirianov, *Phys. Rev. B* **2010**, *82*, 094417; b) E. A. Eliseev, M. D. Glinchuk, V. Khist, V. V. Skorokhod, R. Blinc, A. N. Morozovska, *Phys. Rev. B* **2011**, *84*, 174112; c) S. Sidhardh, M. C. Ray, *J. Appl. Phys.* **2018**, *124*, 244101.
- [10] a) B. A. Belyaev, A. V. Izotov, P. N. Solovev, N. M. Boev, *Phys. Status Solidi RRL* **2020**, *14*, 1900467; b) J. X. Zhang, R. J. Zeches, Q. He, Y. H. Chu, R. Ramesh, *Nanoscale* **2012**, *4*, 6196; c) J. H. Lee, K.-E. Kim, B.-K. Jang, A. A. Ünal, S. Valencia, F. Kronast, K.-T. Ko, S. Kowarik, J. Seidel, C.-H. Yang, *Phys. Rev. B* **2017**, *96*, 064402.
- [11] T. Furukawa, *Phase Transitions* **1989**, *18*, 143.
- [12] R. C. G. Naber, P. W. M. Blom, D. M. d. Leeuw, *J. Phys. D: Appl. Phys.* **2006**, *39*, 1984.
- [13] W. J. Hu, D.-M. Juo, L. You, J. Wang, Y.-C. Chen, Y.-H. Chu, T. Wu, *Sci. Rep.* **2015**, *4*, 4772.
- [14] a) Y. Ishibashi, Y. Takagi, *J. Phys. Soc. Jpn.* **1971**, *31*, 506; b) Y. Wu, X. Li, A. M. Jonas, Z. Hu, *Phys. Rev. Lett.* **2015**, *115*, 267601; c) R. Cai, B. Nysten, Z. Hu, A. M. Jonas, *Appl. Phys. Lett.* **2017**, *110*, 202901.
- [15] a) K. L. Metlov, K. Y. Guslienko, *J. Magn. Magn. Mater.* **2002**, *242-245*, 1015; b) C. A. Ross, M. Hwang, M. Shima, J. Y. Cheng, M. Farhoud, T. A. Savas, H. I. Smith, W. Schwarzacher, F. M. Ross, M. Redjail, F. B. Humphrey, *Phys. Rev. B* **2002**, *65*, 144417.
- [16] D. Sarid, *Scanning Force Microscopy*, Oxford University Press, New York **1994**.
- [17] a) S. Dubois, J. Colin, J. L. Duvail, L. Piraux, *Phys. Rev. B* **2000**, *61*, 14315; b) D.-C. Pham, N. Biziere, G. Melilli, R. Pajon, D. Lacour, L. Bouvot, M. Tabellout, D. Lairez, H.-J. Drouhin, M. C. Clochard, J. E. Wegrowe, *Mater. Res. Express* **2014**, *1*, 045017.
- [18] R. R. Birss, E. W. Lee, *Proc. Phys. Soc.* **1960**, *76*, 502.